

Analysis of phase instabilities in amplitude swing for ultrashort pulse train characterization

CRISTIAN BARBERO,^{1,2,*} ÍÑIGO J. SOLA,^{1,2} AND BENJAMÍN ALONSO^{1,2}

¹*Grupo de investigación en Aplicaciones del Láser y Fotónica (ALF), Universidad de Salamanca, 37008 Salamanca, Spain*

²*Unidad de Excelencia en Luz y Materia Estructuradas (LUMES), Universidad de Salamanca, 37008 Salamanca, Spain*

**cristianbp@usal.es*

Abstract: The temporal dynamics of ultrashort pulses are a fundamental feature in ultrafast optics. These dynamics can often be extracted from a two-dimensional trace consisting of a set of nonlinear spectra, using an iterative algorithm. Typically, the measurement of this trace requires integrating the signal of many pulses, which implies that the trace does not correspond to a single pulse when shot-to-shot variations occur. In this case, the pulse train can be characterized statistically, by a base pulse and a metric that quantifies the instabilities. Here, we demonstrate that the amplitude swing technique is sensitive to instabilities, which manifest as two distinct imprints on the measurement. First, we analyze the terms that compose the amplitude swing signal. Then, we study two parameters to quantify the instabilities, related to a shift in the minima of the trace marginal, and to the filling of the trace minima zones, respectively. Finally, we apply these strategies to characterize simulated unstable pulse trains, using a simple technique.

1. Introduction

The measurement of the temporal amplitude and phase of an ultrashort laser pulse is a fundamental, non-trivial task when dealing with such short events. For this purpose, there is a group of techniques based on encoding the temporal dynamics of the pulse into a two-dimensional map, called trace. This trace often represents the spectrum of a nonlinear signal generated by the tested pulse as a function of a technique-specific parameter, i.e., is the nonlinear intensity as a function of the optical frequency and this parameter. Some representative examples of these techniques are FROG [1], d-scan [2], FROSt [3], and a-swing [4], in which the varying parameter are the delay between both replicas, the dispersion introduced by a previous system, the delay between the pulse and an ultrafast switch, and the relative amplitude between two delayed replicas, respectively. Under ideal conditions, each pulse yields a unique trace, and each trace corresponds to a unique pulse. Thus, from the 2D trace, the pulse amplitude and phase are retrieved using an iterative algorithm, that can be based on projections [5,6], gradient-descent optimization [7–9], evolutionary strategies [10,11], ptychography [12–15], neural networks [16,17], or others [18].

The experimental implementation of these techniques usually involves mechanical scanning to acquire the nonlinear signal while varying the corresponding parameter. Therefore, the detector integrates the signals from many pulses, yielding a trace that is the incoherent superposition of the individual traces of the pulses within the train. Thus, the measured trace will correspond to a single pulse only if all pulses exhibit the same amplitude and phase, which is generally a reasonable assumption in pulse characterization.

However, numerous situations exist in which the temporal profile varies from shot to shot, such as supercontinuum lasers [19]. Under these conditions, the measured trace results from contributions of multiple pulses rather than a single pulse, and thus the retrieval admits no unique solution. There are two approaches to address this: the individual measurement of all pulses within the train or the extraction of statistical information regarding the pulse train. The first approach implies the use of single-shot implementations of these characterization techniques, in which the varying parameter is encoded in a spatial dimension, allowing the

measurement of the trace of a single laser shot [20–23]. Thus, all the pulses within a train can be measured, obtaining the full pulse train dynamics. However, this approach can be impractical under certain circumstances, specifically at low pulse intensity or high repetition rate. A low pulse intensity complicates the generation and detection of the nonlinear signal, while a high repetition rate would require a huge number of measurements and retrievals, requiring extensive computational time and power. Furthermore, increasing the repetition rate implies a shorter integration time to isolate a single pulse, requiring higher peak intensity, and even potentially exceeding the capabilities of typical spectrometers, whose minimum integration time is about 10 μ s (maximum repetition rate of 100 kHz [24]).

Under these circumstances, the second approach, based on statistical analysis, proves to be more practical and efficient. Despite not capturing the full temporal evolution, the pulse train can be characterized by a base pulse and its variability within the train. This approach applies to scanning architecture, and to single-shot modality (in the case of multi-pulse integration). The retrieved information is enough to provide a representative profile of the pulse train and can be helpful to optimize it and to remove the instabilities, undesired in most cases [25]. For this purpose, FROG has previously been applied, modelling the train as a combination of a coherent artifact, the shortest repeatable structure within the train, and an average pulse, a longer pulse whose duration correlates with the degree of pulse variability [26–28]. Similarly, MIIPS was used to study instabilities in mode-locked semiconductor lasers [29]. Later, self-calibrating d-scan [9] was applied to quantify and correct instabilities within an Erbium-doped fiber laser. In this case, the discrepancy between the known dispersion of the compressor and the dispersion value retrieved by the algorithm provides the instability metric [30–32].

In this work, we analyze the impact of shot-to-shot pulse-shape fluctuations on the a-swing trace, providing a useful tool for the characterization of unstable pulse trains, since a-swing can be applied to diverse pulse parameters [11,33,34]. Section 2 presents an in-depth study of the a-swing trace. This study is used to identify instabilities and to understand how pulse information is encoded, potentially enabling improved retrieval strategies. Section 3 introduces a set of five pulse trains exhibiting varying degrees of instability. In Section 4, their traces are computed and retrieved using a ptychographic algorithm [13]. These traces are calculated for two values of the MWP phase retardation (π and 1.5π), since we have found two different imprints of instabilities on the trace, each appearing mainly for one of said MWP phase retardation values. First, for a phase of 1.5π , instabilities manifest as a shift in the minima of the trace marginal (Eq. 7) in θ (the orientation of the MWP), or, equivalently, a modification of the Fourier coefficients (Eq. 5). Second, for a phase of π , a filling of the null-intensity zones is observed, which we quantify studying the distribution of the retrieval error. In both cases, we use an MWP delay equivalent to the Fourier-transform-limited (FTL) pulse duration, which is the optimal value for a-swing retrievals of stable pulse trains [4,33]. In sum, we demonstrate that a-swing is sensitive to fluctuations of the pulse shape along the train, making it a good candidate to temporally characterize both stable and unstable pulse trains.

2. Fourier analysis of a-swing traces

The a-swing setup scans the relative amplitude of two time-delayed replicas of an unknown pulse —assumed here to be horizontally polarized. This inline common-path generation is facilitated by a rotating MWP and a linear polarizer (LP). After this pulse manipulation, the second-harmonic generation (SHG) spectrum is produced in a nonlinear crystal (NL) and measured for each orientation of the MWP θ , i.e., representing relative amplitude, yielding the 2D trace (Fig. 1). The spectral-domain representation of the pulse before the SHG is:

$$E_{LP}(\omega, \theta) = E(\omega) [\cos^2 \theta e^{i \rho_f(\omega)} + \sin^2 \theta e^{i \rho_s(\omega)}] \quad (1)$$

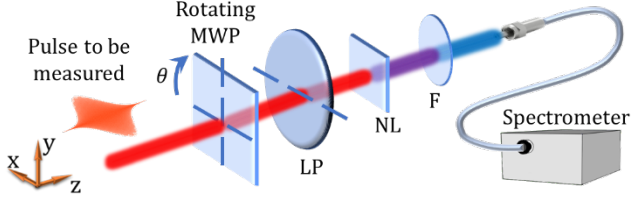


Fig. 1. Amplitude swing conventional experimental setup [4]. Pulse manipulation: multiple-order waveplate (MWP) and linear polarizer (LP). Nonlinear generation and detection: nonlinear crystal (NL), filter of the fundamental signal (F) and spectrometer.

where $E(\omega) = A(\omega) e^{i\varphi(\omega)}$ represents the input pulse, and $\rho_f(\omega)$ and $\rho_s(\omega)$ denote the phases due to the MWP fast and slow axes, respectively. The SHG of this pulse is subsequently calculated as the square of the temporal field profile:

$$E_{\text{SHG}}(\omega, \theta) = \int \left(\int E_{\text{LP}}(\omega, \theta) e^{-i\omega't} d\omega' \right)^2 e^{+i\omega t} dt \quad (2)$$

which can be written as

$$E_{\text{SHG}}(\omega, \theta) = E_{\text{ff}}(\omega) \cos^4 \theta + 2E_{\text{fs}}(\omega) \cos^2 \theta \sin^2 \theta + E_{\text{ss}}(\omega) \sin^4 \theta \quad (3)$$

where $E_{\text{ff}}(\omega)$ and $E_{\text{ss}}(\omega)$ represent the SHG signals of the fast and slow replicas, respectively, and $E_{\text{fs}}(\omega)$ the sum-frequency generation (SFG) between both. Then, the a-swing trace is defined as the modulus square of this SHG field:

$$S_{\text{SHG}}(\omega, \theta) = |E_{\text{SHG}}(\omega, \theta)|^2 = s_{4f}(\omega) \cos^8 \theta + s_{3f,s}(\omega) \cos^6 \theta \sin^2 \theta + s_{2f,2s}(\omega) \cos^4 \theta \sin^4 \theta + s_{f,3s}(\omega) \cos^2 \theta \sin^6 \theta + s_{4s}(\omega) \sin^8 \theta \quad (4)$$

where the subscripts of the s -coefficients indicate the terms of the SHG pulse from which they originate. This expression can be expanded as a Fourier series:

$$S_{\text{SHG}}(\omega, \theta) = a_0(\omega) + a_2(\omega) \cos 2\theta + a_4(\omega) \cos 4\theta + a_6(\omega) \cos 6\theta + a_8(\omega) \cos 8\theta \quad (5)$$

obtaining that the trace presents just even cosine terms up to order 8, since it is symmetric with respect to $\theta = 90^\circ$ and it is periodic every 180° . The equivalence between the s -coefficients and the Fourier coefficients is given by

$$\begin{pmatrix} s_{4f}(\omega) \\ s_{3f,s}(\omega) \\ s_{2f,2s}(\omega) \\ s_{f,3s}(\omega) \\ s_{4s}(\omega) \end{pmatrix} = \begin{pmatrix} +1 & +1 & +1 & +1 & +1 \\ +4 & +2 & -4 & -14 & -28 \\ +6 & 0 & -10 & 0 & +70 \\ +4 & -2 & -4 & +14 & -28 \\ +1 & -1 & +1 & -1 & +1 \end{pmatrix} \begin{pmatrix} a_0(\omega) \\ a_2(\omega) \\ a_4(\omega) \\ a_6(\omega) \\ a_8(\omega) \end{pmatrix} \quad (6)$$

The frequency-dependent Fourier coefficients can be directly obtained from the trace, without knowing the pulse, thus we can also calculate the s -coefficients before the retrieval, which will provide preliminary information about the pulse, such as the sign of the phase. Furthermore, we will use the trace marginals $M_\omega(\omega)$ and $M_\theta(\theta)$, that result from integrating the trace across its two axes, and are related with the Fourier coefficients by:

$$\begin{aligned} M_\omega(\omega) &= \int_0^\pi S_{\text{SHG}}(\omega, \theta) d\theta = \sum_{n=0}^4 \left(a_{2n}(\omega) \int_0^\pi \cos 2n\theta d\theta \right) = \pi a_0(\omega) \\ M_\theta(\theta) &= \int_{-\infty}^{+\infty} S_{\text{SHG}}(\omega, \theta) d\omega = \sum_{n=0}^4 \left(\cos 2n\theta \int_{-\infty}^{+\infty} a_{2n}(\omega) d\omega \right) \end{aligned} \quad (7)$$

From these expressions, we conclude that the offset term $a_0(\omega)$ is proportional to the frequency marginal, as expected, since it is not modulated by θ . We can also deduce that $a_2(\omega) = -a_6(\omega)$, since the intensity must be identical at the orientations where only a single replica exists, $\theta = 0, 90, 180^\circ$ (considering that the MWP relative dispersion is small within the pulse bandwidth). Furthermore, we can deduce the relation between the coefficients of two pulses with conjugated spectral phases, $a_2^{(\varphi)}(\omega) = -a_2^{(-\varphi)}(\omega)$, which means that the traces of these phase-conjugate pulses are shifted by 90° between them.

3. Simulation of the unstable pulse trains

To simulate the set of unstable pulse trains, a base pulse has been initially defined with a Gaussian spectrum centered at 800 nm, presenting a FTL duration of 50 fs, and a spectral phase given by -3000 fs^2 of group delay dispersion (GDD) and $+10^5 \text{ fs}^3$ of third-order dispersion (TOD) (Fig. 2). These parameters were chosen to match realistic experimental conditions, while the observed qualitative behavior does not depend on their exact values. To this base pulse, we add random variations to the spectral phase, without modifying the spectrum, resulting in five trains of 101 different pulses each. A similar methodology to construct the pulse trains has been employed in previous works with FROG and d-scan [25,26,30,31]. Thus, each pulse within the train is defined by the spectrum of the base pulse and a spectral phase $\varphi_i(\omega)$ expressed as:

$$\varphi_i(\omega) = \frac{-3000 \text{ fs}^2}{2}(\omega - \omega_0)^2 + \frac{10^5 \text{ fs}^3}{6}(\omega - \omega_0)^3 + \alpha \cdot \mathcal{U}_\omega(-\pi, \pi) \quad (8)$$

where ω_0 denotes the central frequency and α is the parameter governing the degree of instability. This instability is introduced via a function \mathcal{U}_ω that assigns independent random values to the phase of each frequency component. After this, the phase is smoothed by applying a super-Gaussian temporal filter (order 3, width 1200 fs) to remove noise at temporal delays far from the pulse peak. Following this procedure, we defined five pulse trains corresponding to $\alpha = [0.15, 0.30, 0.45, 0.60, 0.75]$ (Fig. 3). Tab. 1 summarizes the statistical parameters of each train in terms of the full width at half maximum (FWHM) and second moment (SM) pulse durations. The former reflects the duration of the most intense peak, while the latter considers the secondary temporal structure of the pulse, i.e., it serves a measure of the temporal spreading (it corresponds to the $1/e^2$ width in the case of a Gaussian profile). The train preserves the main features of the base pulse for $\alpha \leq 0.45$, while for greater values, especially for $\alpha = 0.75$, this structure presents significant degradation.

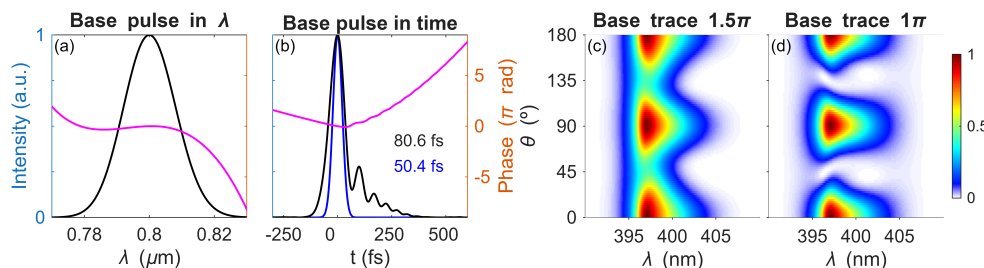


Fig. 2. Base pulse in: (a) wavelengths; (b) time, with the FTL pulse in blue and the FWHM durations indicated. Black and blue: intensity; magenta: phase. Simulated traces for MWP phase retardation equal to: (c) 1.5π ; (d) π . The MWP delay is 50 fs in both cases.

Table 1. Statistics of pulse durations of the different pulse trains. The FWHM and SM durations of the base pulse ($\alpha = 0$) are 80.6 and 188.7 fs, respectively.

	$\alpha = 0.15$		$\alpha = 0.30$		$\alpha = 0.45$		$\alpha = 0.60$		$\alpha = 0.75$	
	FWHM	SM	FWHM	SM	FWHM	SM	FWHM	SM	FWHM	SM
Mean (fs)	81.5	191.9	81.6	213.3	81.0	263.1	82.1	367.58	84.22	516.72
Mean / base	1.01	1.02	1.01	1.13	1.01	1.39	1.02	1.95	1.05	2.74
std / mean (%)	3.62	2.02	7.49	5.29	10.90	10.73	18.41	19.26	34.57	19.2
Norm var (%)	0.13	0.04	0.56	0.28	1.19	1.15	3.39	3.71	11.95	3.69

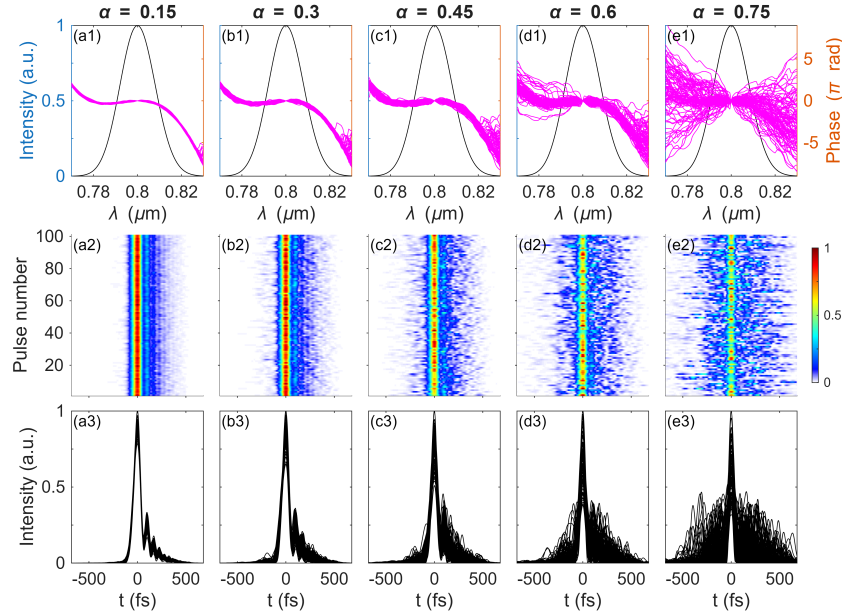


Fig. 3. Unstable pulse trains for: (a) $\alpha = 0.15$; (b) $\alpha = 0.3$; (c) $\alpha = 0.45$; (d) $\alpha = 0.6$; (e) $\alpha = 0.75$. Row 1: spectrum (black) and spectral phases (magenta); Rows 2 and 3: temporal intensities (indicated by the color bar in row 2; black curves in row 3).

4. Amplitude swing unstable pulse train retrievals

In this section, we present the simulated a-swing traces of the previously mentioned pulse trains (Fig. 3), using two 1.6-mm-thick MWPs of α -quartz. The birefringence and thickness of the plate produce a 50-fs delay, corresponding to the FTL pulse duration, as well as a multi-order retardation. To indicate its value, the $2\pi m$ offset is removed, and only the zero-order relative phase is reported in the phase retardation, which, unless specified otherwise, refers to the central frequency (the dephasing of the MWP is chromatic). Since we have observed two manifestations of instabilities depending on the phase retardation, we choose the values π and 1.5π for the trace simulations, i.e., half-wave plate (HWP) and quarter-wave plate (QWP) operation. These traces have been reconstructed using the ptychographic algorithm developed for a-swing in Ref. [13]. We present the retrieved pulses for different degrees of phase instability, and we propose two metrics to quantify these instabilities, allowing to distinguish between stable and unstable pulse trains.

4.1 Retrievals of traces with MWP acting as a QWP

In the case of an MWP phase retardation of 1.5π (for 800 nm), the marginal in θ is modified by instabilities due to variations in the Fourier coefficients $a_2(\omega)$ and $a_6(\omega)$ (they have opposite sign). As α increases, the deviation between the base trace and the trace of the unstable pulse train grows, as expected. For $\alpha = 0.15$ and $\alpha = 0.3$, the trace barely changes, thus the algorithm retrieves the base pulse. For higher instability values, the retrieved pulses progressively lose their secondary structure, while retrieving well the main pulse peak (Fig. 4). Even in the case of maximum instability, where the simulated traces significantly differ from the base trace, the G error (Eq. 9) remains below 2%, as the main differences arise in the zones of null intensity. Thus, this error is not an adequate metric to detect and quantify instabilities since one may confuse a stable train of clean pulses with an unstable pulse train of very structured pulses. Fortunately, instabilities clearly manifest by modifying the Fourier coefficients $a_2(\omega)$ and $a_6(\omega)$, which is translated in this case as a shift of the minima of the marginal M_θ (Fig. 5).

$$G = \frac{1}{N_\omega N_\theta} \sqrt{\sum_{\omega, \theta} (S_{\text{SHG}}^{\text{retr}}(\omega, \theta) - S_{\text{SHG}}^{\text{sim}}(\omega, \theta))^2} \quad (9)$$

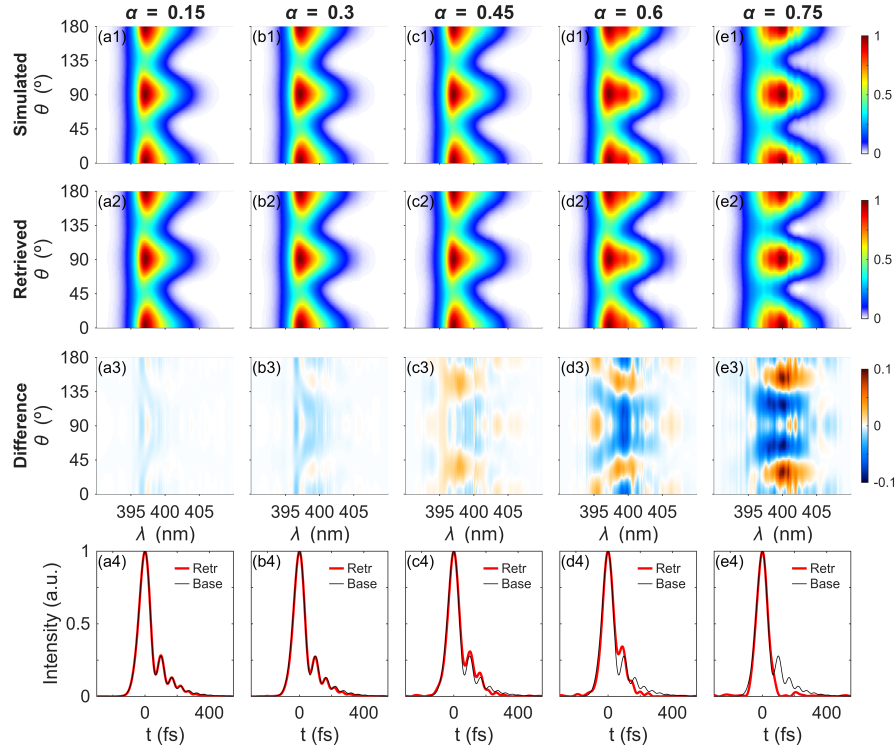


Fig. 4. Retrievals for MWP operating as a QWP, with phase retardation of 1.5π : (a) $\alpha = 0.15$; (b) $\alpha = 0.3$; (c) $\alpha = 0.45$; (d) $\alpha = 0.6$; (e) $\alpha = 0.75$. Row 1: simulated traces; Row 2: retrieved traces; Row 3: difference; Row 4: retrieved pulses in time domain.

We propose the following metric, Γ_{QWP} , to quantify pulse train instabilities:

$$\Gamma_{\text{QWP}} = 1 - \frac{a_{2,\text{sum}}^{\text{sim}}}{a_{2,\text{sum}}^{\text{retr}}} = 1 - \frac{\int a_2^{\text{sim}}(\omega) d\omega}{\int a_2^{\text{retr}}(\omega) d\omega} \quad (10)$$

This parameter yields a value of 0 in the absence of instabilities, and it approaches 1 as the instabilities increase. A value exceeding 1 would indicate that the signs of $a_{2,sum}^{retr}$ and $a_{2,sum}^{sim}$ are opposite, implying that the algorithm has converged to a local solution where the pulse has the phase conjugate of the correct solution, as deduced at the end of Section 2.

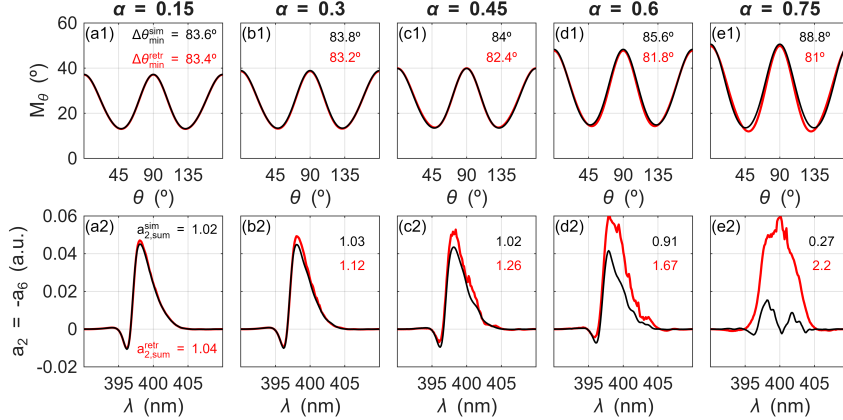


Fig. 5. Effect of pulse-train instabilities for a phase retardation of 1.5π . Row 1: Simulated (black) and retrieved (red) marginals, with the distance between minima indicated; Row 2: simulated (black) and retrieved (red) second Fourier coefficient $a_2(\omega)$, where the inset indicates the corresponding integrated values. (a) $\alpha = 0.15$; (b) $\alpha = 0.3$; (c) $\alpha = 0.45$; (d) $\alpha = 0.6$; (e) $\alpha = 0.75$.

4.2 Retrievals of traces with MWP acting as an HWP

In the case of an MWP phase retardation of π (for 800 nm), instabilities have a similar impact on the simulated and retrieved traces and pulses than the case of 1.5π . For low levels of instability, the simulated trace is almost equal to the base trace, and thus the retrieved pulse agrees with the base pulse. For higher instability values, the simulated traces are different, but the algorithm is still able to find an apparently convincing solution. As previously mentioned, the error is located mainly within the trace zones of minimum intensity, so the G error remains low even under high instability values (Fig. 6). Furthermore, in the case of symmetric spectral amplitude and phase, an MWP phase retardation of π results in a marginal that is periodic every 90° (equivalently, exhibiting symmetry with respect to 45° and 135°); as a result, the integral of the second and sixth Fourier coefficients is null. In our case, the TOD slightly breaks that symmetry and thus said Fourier coefficients are approximately zero (Fig. 7, Rows 1 and 2). For this reason, the shift of the marginal minima and the parameter Γ_{QWP} are not reliable indicators in this configuration. One alternative is to analyze the Fourier coefficients as a function of frequency, which do show variations, although these changes are smaller than in the case of 1.5π . Thus, a more reliable indicator is required.

To this end, we create a modified trace $S_{norm}(\omega, \theta)$ by normalizing each nonlinear spectrum of the trace (i.e., each trace slice for every θ value). This approach enhances the contribution of the zones of lower intensity. Then, we compare the retrieval error of the raw trace (G_{raw} , Eq. 9) with the retrieval error of the normalized trace (G_{norm} , comparing S_{norm}^{retr} and S_{norm}^{sim}) for the different degrees of instability. While increasing the instabilities, G_{raw} and G_{norm} grow at very different rates, enhancing their difference. Therefore, pulse instabilities can be estimated using the following metric:

$$\Gamma_{\text{HWP}} = \frac{G_{\text{norm}} - G_{\text{raw}}}{G_{\text{norm}} + G_{\text{raw}}} \quad (11)$$

Since the traces of the different pulses within the instable train present null intensity at different positions, their incoherent superposition will produce traces without areas with zero intensity. To further quantify this behavior, we computed the G errors after truncating the traces at an intensity threshold $0 < S_{\text{th}} < 1$ defined by $S_{\text{SHG}}(S_{\text{SHG}} < S_{\text{th}}) = S_{\text{th}}$, which provides information about how the retrieval error is distributed (Fig. 7, Row 3). In addition, we calculate the derivative of G with respect to this threshold, which can be used as a complementary indicator of instabilities (Fig. 7, Row 4).

Importantly, this indicator discriminates between pulse-shape instabilities and stable pulse trains in the presence of experimental noise or intensity fluctuations during the scan. On one hand, experimental noise causes a retrieval G error that would be a priori uniformly distributed along the different intensities of the trace. Thus, upon increasing noise, both G_{norm} and G_{raw} grow at similar rates and their difference remains low. On the other hand, in the case of pure energy fluctuations, the spectra of the retrieved trace have the same shape but different amplitude than that of the simulated/experimental trace. Therefore, G_{norm} is smaller than G_{raw} , since the normalization forces the amplitude agreement, and Γ_{HWP} would be negative.

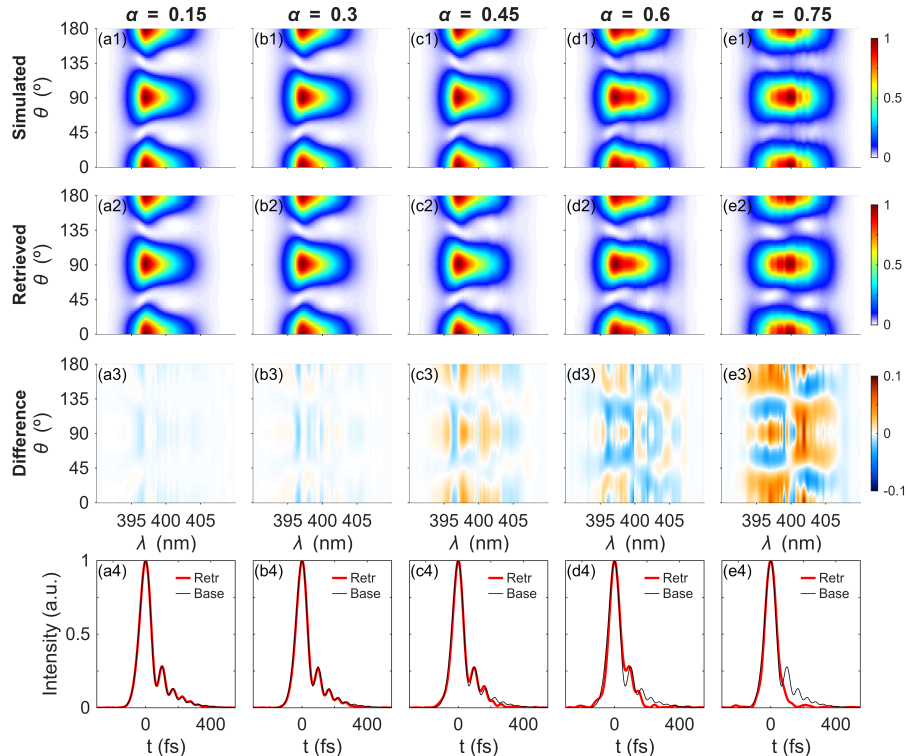


Fig. 6. Retrievals for MWP operating as a HWP, with phase retardation of π : (a) $\alpha = 0.15$; (b) $\alpha = 0.3$; (c) $\alpha = 0.45$; (d) $\alpha = 0.6$; (e) $\alpha = 0.75$. Row 1: simulated traces; Row 2: retrieved traces; Row 3: difference; Row 4: retrieved pulses in the temporal domain.

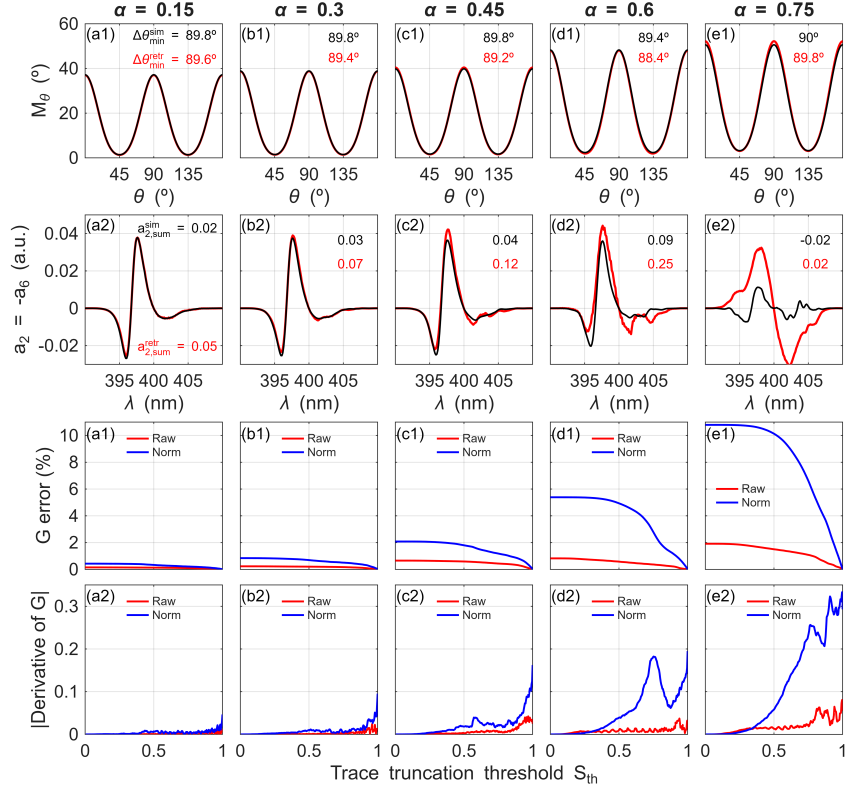


Fig. 7. Imprints of instabilities for a phase retardation of π . Row 1: Simulated and retrieved marginals; Row 2: simulated and retrieved second Fourier coefficient. Row 3: G error of the raw and normalized traces as a function of the truncation threshold S_{th} . Row 4: derivative of the G errors respect to this threshold. (a) $\alpha = 0.15$; (b) $\alpha = 0.3$; (c) $\alpha = 0.45$; (d) $\alpha = 0.6$; (e) $\alpha = 0.75$.

4.3 Arbitrary MWP phase retardation

The a-swing traces of unstable pulse trains, calculated for any MWP phase retardation, present the two discussed effects. Depending on the MWP phase retardation, their respective prominence will vary. As discussed above, these effects manifest by modifying the frequency-dependent Fourier coefficients (which can shift the marginal minima) and by filling the null-intensity regions of the trace, which increases the error in these specific zones of the trace. The first effect is most pronounced when the MWP phase is near to 1.5π (or 0.5π) and becomes less pronounced as it approaches π and 2π . Conversely, the second effect is most evident as the MWP phase approaches π , since there are more regions where destructive interference occurs within the trace. Considering this, a phase retardation far from 0 or 2π , where both effects are minimal, should be chosen to be more sensitive to instabilities.

5. Conclusion

We have shown how pulse train instabilities manifest in the amplitude swing trace, presenting two different effects and consequently proposing two corresponding strategies and metrics to quantify these instabilities. The prominence of these two phenomena on the amplitude swing trace depends on the phase retardation of the rotating multiple-order waveplate used for the manipulation of the pulse.

First, we have explored the constituent terms that compose the trace, decomposing it as a Fourier series with only even cosine terms up to eighth order. Then, we simulated a set of five pulse trains characterized by varying degrees of spectral phase instabilities. The traces of these pulse trains were simulated and retrieved, revealing that the second- and sixth-order frequency-dependent terms, $a_2(\omega)$ and $a_6(\omega)$, which are opposite, are modified by the presence of instabilities, yielding a metric to quantify them, Γ_{QWP} . The second metric, Γ_{HWP} , is based on the distribution of the retrieval G error. Since instabilities are mainly manifested in the zones of minimum intensity within the trace, the retrieval G error is not appreciably affected by instabilities and therefore is not a sufficiently sensitive metric. To address this, we normalized each spectrum of the trace by its individual maximum intensity, enhancing the contribution of the lowest intensity zones. This procedure enables a comparison of the retrieval errors between the raw and normalized traces, G_{raw} and G_{norm} , providing a second metric for quantifying instabilities, Γ_{HWP} .

This analysis is especially useful for low-intensity, high-repetition-rate systems, where measuring every individual pulse is highly impractical. While this study focuses on scalar pulses with constant linear polarization using the conventional amplitude swing configuration, the transition to the generalized setup, or the inclusion of vectorial pulses with time-dependent polarization, reveal a more complex trace structure. In such cases, additional terms emerge within the signal, necessitating further investigation into future work.

In conclusion, we demonstrate that amplitude swing can distinguish between stable and unstable pulse trains, providing a simple and versatile tool to characterize ultrashort pulse trains presenting temporal profiles that vary shot to shot.

Funding. Ministerio de Ciencia, Innovación y Universidades (PID2023-149836NB-I00); Consejería de Educación, Junta de Castilla y León (SA108P24, Escalera de Excelencia CLU-2023-1-02); European Regional Development Fund.

Acknowledgments. C. Barbero acknowledges the support from Junta de Castilla y León and Fondo Social Europeo Plus through their Ph. D. grant program.

Disclosures. B. Alonso and I. J. Sola have patent # WO/2021/123481 pending to University of Salamanca.

Data availability. Data underlying the results presented in this paper are not publicly available at this time but may be obtained from the authors upon reasonable request.

References

1. D. J. Kane and R. Trebino, "Characterization of arbitrary femtosecond pulses using frequency-resolved optical gating," *IEEE J. Quantum Electron.* **29**, 571–579 (1993).
2. M. Miranda, T. Fordell, C. Arnold, A. L'Huillier, and H. Crespo, "Simultaneous compression and characterization of ultrashort laser pulses using chirped mirrors and glass wedges," *Opt. Express* **20**, 688–697 (2012).
3. A. Leblanc, P. Lassonde, S. Petit, J.-C. Delagnes, E. Haddad, G. Ernotte, M. R. Bionta, V. Gruson, B. E. Schmidt, H. Ibrahim, E. Cormier, and F. Légaré, "Phase-matching-free pulse retrieval based on transient absorption in solids," *Opt. Express* **27**, 28998–29015 (2019).
4. B. Alonso, W. Holgado, and I. J. Sola, "Compact in-line temporal measurement of laser pulses with amplitude swing," *Opt. Express* **28**, 15625–15640 (2020).

5. D. J. Kane, "Principal components generalized projections: a review [Invited]," *J. Opt. Soc. Am. B* **25**, A120–A132 (2008).
6. M. Miranda, J. Penedones, C. Guo, A. Harth, M. Louisy, L. Neorićić, A. L’Huillier, and C. L. Arnold, "Fast iterative retrieval algorithm for ultrashort pulse characterization using dispersion scans," *J. Opt. Soc. Am. B* **34**, 190–197 (2017).
7. N. C. Geib, M. Zilk, T. Pertsch, and F. Eilenberger, "Common Pulse Retrieval Algorithm: A Fast and Universal Method to Retrieve Ultrashort Pulses," *Optica* **6**, 495–505 (2019).
8. M. Jasiulek, "Solving nonlinear integral equations for laser pulse retrieval with Newton’s method," *Phys. Rev. E* **103**, 053306 (2021).
9. B. Alonso, I. J. Sola, and H. Crespo, "Self-calibrating d-scan: measuring ultrashort laser pulses on-target using an arbitrary pulse compressor," *Sci. Rep.* **8**, 3264 (2018).
10. E. Escoto, A. Tajalli, T. Nagy, and G. Steinmeyer, "Advanced phase retrieval for dispersion scan: a comparative study," *J. Opt. Soc. Am. B* **35**, 8–19 (2018).
11. M. López-Ripa, I. J. Sola, and B. Alonso, "Amplitude swing ultrashort pulse characterization across visible to near-infrared," *Opt. Laser Technol.* **164**, 109492 (2023).
12. P. Sidorenko, O. Lahav, Z. Avnat, and O. Cohen, "Ptychographic reconstruction algorithm for frequency-resolved optical gating: super-resolution and supreme robustness," *Optica* **3**, 1320–1330 (2016).
13. C. Barbero, I. J. Sola, and B. Alonso, "Ptychographic retrieval for complete ultrashort pulse amplitude swing reconstruction," *Opt. Laser Technol.* **188**, 112939 (2025).
14. T. Gomes, M. Canhota, and H. Crespo, "Temporal characterization of broadband femtosecond laser pulses by a surface third-harmonic dispersion scan with a ptychographic retrieval," *Opt. Lett.* **47**, 3660–3663 (2022).
15. D. Spangenberg, P. Neethling, E. Rohwer, M. H. Brügmann, and T. Feurer, "Time-domain ptychography," *Phys. Rev. A* **91**, 021803(R) (2015).
16. S. Kleinert, A. Tajalli, T. Nagy, and U. Morgner, "Rapid phase retrieval of ultrashort pulses from dispersion scan traces using deep neural networks," *Opt. Lett.* **44**, 979–982 (2019).
17. T. Zahavy, A. Dikopoltsev, D. Moss, G. I. Haham, O. Cohen, S. Mannor, and M. Segev, "Deep learning reconstruction of ultrashort pulses," *Optica* **5**, 666–673 (2018).
18. C. Oxelmark Krook and V. Pasiskevicius, "Overcoming noise in pulse retrieval: introducing the line-search FROG algorithm," *Opt. Express* **33**, 33258–33269 (2025).
19. B. Schenkel, R. Paschotta, and U. Keller, "Pulse compression with supercontinuum generation in microstructure fibers," *J. Opt. Soc. Am. B* **22**, 687–693 (2005).
20. D. J. Kane and R. Trebino, "Single-shot measurement of the intensity and phase of an arbitrary ultrashort pulse by using frequency-resolved optical gating," *Opt. Lett.* **18**, 823–825 (1993).
21. D. Fabris, W. Holgado, F. Silva, T. Witting, J. W. G. Tisch, and H. Crespo, "Single-shot implementation of dispersion-scan for the characterization of ultrashort laser pulses," *Opt. Express* **23**, 32803–32808 (2015).
22. B. Brizard, A. Leblanc, S. Petit, J.-C. Delagnes, É. Cormier, H. Ibrahim, F. Légaré, and P. Lassonde, "Single-shot phase-matching free ultrashort pulse characterization based on transient absorption in solids," *Opt. Express* **28**, 35807–35815 (2020).
23. C. Barbero, I. J. Sola, and B. Alonso, "Ultrafast single-shot amplitude swing pulse measurement," *J. Phys. Photonics* **7**, 035028 (2025).
24. W. Hao, X. Liu, Z. Yang, M. Mao, and Y. Tang, "Time-delay Fourier transform spectrometer for high-speed spectral measurement," *Opt. Commun.* **560**, 130483 (2024).
25. J. Ratner, G. Steinmeyer, T. C. Wong, R. Bartels, and R. Trebino, "Coherent artifact in modern pulse measurements," *Opt. Lett.* **37**, 2874–2876 (2012).
26. M. Rhodes, G. Steinmeyer, J. Ratner, and R. Trebino, "Pulse-shape instabilities and their measurement," *Laser Photon. Rev.* **7**, 557–565 (2013).
27. Y. Li, L. F. Lester, D. Chang, C. Langrock, M. M. Fejer, and D. J. Kane, "Characteristics and instabilities of mode-locked quantum-dot diode lasers," *Opt. Express* **21**, 8007–8017 (2007).
28. M. López-Ripa, B. Alonso, S. Jarabo, F. J. Salgado-Remacha, J. C. Aguado, and I. J. Sola, "Coherent artifact and time-dependent polarization in amplified ultrafast erbium-doped fibre lasers," *Opt. Laser Technol.* **140**, 107018 (2021).

29. V. V. Lozovoy, G. Rasskazov, D. Pestov, and M. Dantus, "Quantifying noise in ultrafast laser sources and its effect on nonlinear applications," *Opt. Express* **23**, 12037–12044 (2015).
30. E. Escoto, D. Gerth, B. Hofmann, and G. Steinmeyer, "Strategies for the characterization of partially coherent ultrashort pulses with dispersion scan," *J. Opt. Soc. Am. B* **36**, 2092–2098 (2019).
31. B. Alonso, S. Torres-Péiró, R. Romero, P. T. Guerreiro, A. Almagro-Ruiz, H. Muñoz-Marco, P. Pérez-Millán, and H. Crespo, "Detection and elimination of pulse train instabilities in broadband fibre lasers using dispersion scan," *Sci. Rep.* **10**, 7242 (2020).
32. T. dos S. Gomes, B. Alonso, H. Crespo, and M. A. Cataluna, "Quantification of pulse train instabilities in mode-locked quantum-dot laser diodes," in *CLEO 2024* (Optica Publishing Group, 2024), p. JTU2A.29.
33. I. J. Sola and B. Alonso, "Robustness and capabilities of ultrashort laser pulses characterization with amplitude swing," *Sci. Rep.* **10**, 18364 (2020).
34. M. López-Ripa, Ó. Pérez-Benito, B. Alonso, R. Weigand, and I. J. Sola, "Few-cycle pulse retrieval using amplitude swing technique," *Opt. Express* **32**, 21149–21159 (2024).